ACS APPLIED MATERIALS & INTERFACES

www.acsami.org

Research Article

Sensitive Thermography via Sensing Visible Photons Detected from the Manipulation of the Trap State in $MAPbX_3$

Yubing Xu, Xin Wang, Shilin Liu, Yuzhu Pan, Abida Perveen, Damian Chinedu Onwudiwe, Omolola Esther Fayemi, Elias Emeka Elemike, Byung Seong Bae, Ying Zhu, Razika Zair Talaighil, Xiaobing Zhang, Jing Chen, Zhiwei Zhao, Qing Li, Wei Lei,* and Xiaobao Xu*

Cite This: *ACS Appl. Mater. Interfaces* 2023, 15, 56526−56536

Read Online

ACCESS | Metrics & More | Article Recommendations | Supporting Information

ABSTRACT: Sensitive thermometry or thermography by responding to blackbody radiation is urgently desired in the intelligent information life, including scientific research, medical diagnosis, remote sensing, defense, etc. Even though thermography techniques based on infrared sensing have undergone unprecedented development, the poor compatibility with common optical components and the high diffraction limit impose an impediment to their integration into the established photonic integrated circuit or the realization of high-spatial-resolution and high-thermal-resolution imaging. In this work, we present a sensitive temperature-dependent visible photon detection in Bi-doped $MAPbX_3$ (X = Cl, Br, and I) and employ it for uncooled thermography. Systematic measurements reveal that the Bi dopant introduces trap states in $MAPbX_3$, thermal energy facilitates the carriers jumping from trap states to the conduction band, while the vacancies of trap states ensure the sequential absorption of visible photons with energy less than the band gap. Subsequently, the change of response toward the visible photon is applied to construct the thermograph, and it possesses a specific sensitivity of 2.11% K^{-1} along temperature variation. As a result, our thermograph presents a temperature resolution of 0.21 nA K^{-1}, a high responsivity of 2.06 mA W^{-1}, and a high detectivity of 2.08×10^9 Jones at room temperature. Furthermore, remote thermal imaging is successfully achieved with our thermograph.

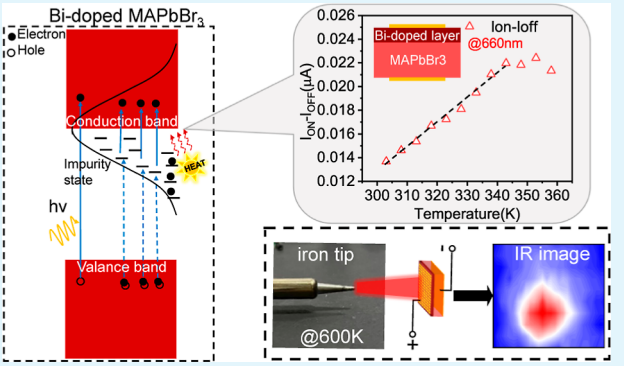

KEYWORDS: *thermograph, photodetector, perovskite, Bi-$MAPbBr_3$, single crystal*

INTRODUCTION

Beyond visible or near-infrared photons, the acquisition of thermal radiation from the target can provide more identifiable details under weak visible light conditions disregarding disturbance from the normal background.[1,2] Benefiting from this merit, until now, thermal sensing techniques have been intensely explored in many fields, for example, night vision,[3] medical science,[4,5] electronic systems,[6] security,[7] and artificial intelligence.[8] Especially, as the electric car and computational power undergo extraordinary splendor in recent years, thermal detection is showing increasing importance in their intelligent safety systems for ensuring the safety in battery packs, server clusters, etc.[9] Even though it is well-known that the thermal radiation is an infrared (IR) electromagnetic wave and the detection of IR photons can be used to acquire thermal information since the temperature variation can induce the change in IR emission according to the blackbody radiation law

$$B(T)=\sigma T^4 \quad (1)$$

where σ is the Stefan−Boltzmann constant and T is the temperature,[10,11] the detection of the radiative IR photon still faces a challenge due to its feeble energy.

In general, the technique for the realization of thermography can be categorized into two types: photoelectric effect and photothermal effect.[1,12] For the photoelectric effect, it uses the photodetectors with a narrow-bandgap semiconductor (InSb, $In_{1-x}Ga_xAs$, and $Hg_{1-x}Cd_xTe$) or a GaAs/AlGaAs quantum well to respond to the IR photon radiation.[13,14] In this case, the photodetectors convert the IR photon into the electric signal directly with a high response speed. However, because the band gap of active materials is even lower than that of thermal energy at room temperature, the detection of IR photons under room temperature requires additional cryogenic cooling

Received: September 7, 2023
Revised: November 13, 2023
Accepted: November 15, 2023
Published: November 28, 2023

units to suppress the air thermal energy pumping the carrier to the conduction band, which inevitably increases the cost and complexity in devices and subsequently imposes an impediment for its universal application. As a consequence, thermography with an IR photodetector is mainly used in scientific or military equipment.

Alternatively, the photothermal effect including bolometric, thermoelectric, and pyroelectric effects provides another option for constructing the affordable thermograph.[15] In this approach, the thermal sensing materials absorb IR radiation and convert its thermal energy into detectable signals, including electric or photon signals. For instance, Jiang et al. reported conductivity−temperature dependence in GeTe,[16] Reihani et al. reported that GaAs exhibits temperature-dependent reflectance at the chosen wavelength,[17] and our previous work confirms the conductivity−temperature dependence in perovskite materials.[18] All of these attempts demonstrate success in thermal detection. However, it is worth noting that although the photothermal effect empowers the thermal imagery without cooling equipment, it suffers from a slow response speed.

Ultimately, the most important technical challenge facing in both photoelectric effect- and photothermal effect-based thermography is that they cannot be compatible with the conventional optical system due to the poor transmission of thermal energy through the optical component.[17,19] Notably, their integration into the established optical system is extremely essential in realizing high-resolution imaging. Hence, together with their severe diffraction, the thermographic performance is still far from satisfactory due to the limitation in spatial resolution and thermal resolution. Thus, the technique of tracing the change in fluorescence or its lifetimes has been exploited and regarded as a potential way to achieve high-performance nanoscale thermography.

Profiting from the prosperity of development in novel temperature-sensitive materials, Neumann and his co-authors used single defects in diamonds to detect small and local temperature changes.[20] Yakunin et al. presented the strong temperature dependence of the luminescence lifetime of perovskite-like tin halides.[1] Besides, some other perovskites, especially those exhibiting thermoelectric characteristics, their application in thermal detection have also been successfully demonstrated.[21,22] Even so, the stringent requirement on the complicated measurement system still imposes restrictions on their practical application. So, developing feasible and sensitive thermography is still a great desire and challenge for the scientific, industrial, and even military fields.

In this work, we report sensitive thermography with Bi-doped $MAPbX_3$ (Bi-$MAPbX_3$) as a temperature-active material. The dopant of Bi in $MAPbX_3$ induces the traps, resulting in the extra absorption of photons with energy less than the optical band gap. Moreover, the trapped carriers can be pumped to the conduction band by the thermal energy. Thus, the trap and detrap processes lead to the change in the absorption of the tailing photon at different temperatures, which enables the potential in thermal detection with the common photodetector mode. To construct this thermograph and boost its performance, a p−n junction with Bi-$MAPbX_3$ on $MAPbX_3$ was fabricated to enhance the charge carrier transport and collection with Au as electrodes. As a result, our thermograph by responding to visible photons shows an excellent temperature sensitivity of 2.11% K^{-1}, a high thermal resolution of 0.21 nA T^{-1}, a high responsivity of 0.23 mA W^{-1}, and long-term stability. With the assistance of our thermograph, remote thermal imaging of soldering iron with >2 μm IR wave radiation is successfully achieved.

EXPERIMENTAL SECTION

Materials. Lead chloride ($PbCl_2$, 99%) and lead bromine ($PbBr_2$, 98%) were purchased from Sigma-Aldrich, USA. Methylammonium chloride (MACl) and methylammonium bromide (MABr) were purchased from Sigma-Aldrich, USA.

Bismuth chloride ($BiCl_3$, 99.9%) and bismuth bromide ($BiBr_3$, 99%) were purchased from Sigma-Aldrich, USA. Dimethyl sulfoxide (DMSO) and dimethylformamide-d_7 (DMF) were obtained from Aladdin, China. All commercial products were used as received.

Precursor Preparation. For intrinsic $MAPbCl_3$ precursor solution preparation, 1 mol L^{-1} MACl and 1 mol L^{-1} $PbCl_2$ were dissolved in the mixed solution of 50 mL of DMF and 10 mL of DMSO. For intrinsic $MAPbBr_3$ precursor solution preparation, 1 mol L^{-1} MABr and 1 mol L^{-1} $PbBr_2$ were dissolved in 60 mL of DMF. Additionally, to obtain the Bi-doped perovskite precursor, 0.1 mol L^{-1} $BiCl_3$ and 0.1 mol L^{-1} $BiBr_3$ were added into the intrinsic $MAPbCl_3$ and $MAPbBr_3$ perovskite precursor solutions, respectively, which were stirred at room temperature for 2 h.

Device Fabrication. The inverse temperature crystallization (ITC) method was used here to grow Bi-doped and intrinsic $MAPbCl_3$ and $MAPbBr_3$ single crystals (SCs). The intrinsic $MAPbCl_3$ precursor solution and Bi-$MAPbCl_3$ precursor solution were heated from 40 to 60 °C at the speed of 1 °C per 3 h to grow SCs.

Additionally, the intrinsic $MAPbBr_3$ precursor solution and Bi-$MAPbBr_3$ precursor solution were heated from 60 to 80 °C at the speed of 1 °C per 3 h to grow crystals. The solution-processed epitaxial (SPE) growth method was used to grow Bi-$MAPbBr_3$ layers by digging intrinsic $MAPbBr_3$ SCs into the precursor with the Bi-$MAPbBr_3$ precursor solution. After the SPE growth process, the perovskite SCs with a core−shell structure were cut by a diamond wire (Φ 0.35 mm) and were polished by diamond powder (Φ 0.5 μm) and toluene mixed solution. The cutting and polishing machines (STX-202A and UNIPOL-1203) were obtained from Shenyang Kejing Autoinstrument Co., Ltd. (Shenyang, China). What is more, the gold electrodes were deposited on the opposite surface of perovskite SCs in vacuum.

Material Characterization. The samples were held in the larger chamber of INSTEC's HCS402 (USA), which has dual top−bottom heating for reduced vertical temperature gradients, and the high precision thermal control was realized by INSTEC mK2000 (USA). The temperature-dependent absorption of Bi-doped perovskite SCs was measured by a monochromator (Omin-λ200i, Zolix) and a silicon PIN photodiode (S12158-01CT, Hamamatsu) with power supplied by Keithley 2400. The photoluminescence (PL) decay processes were characterized with a SpectraMax instrument (UK). X-ray photoelectron spectroscopy (XPS) was performed by a PHI 5000 Versa Probe (Japan), and X-ray diffraction (XRD) patterns were obtained by an X'TRA system with a Cu target (Switzerland). The contact potential difference was measured by a Kelvin probe force microscopy (KPFM) system from Multimode-8-AM (USA), and the major carrier density was measured by a Hall effect measurement system (PM-50 MR Platform, EMT-2400 Data Acquisition System).

Device Measurement. Scanning electron microscopy (SEM) images were taken with a Quanta 200 FEI (USA), transmission electron microscopy (TEM) images were obtained by a Titan 80-300 FEI (USA), and high-resolution TEM (HR-TEM) images were obtained by a JEM-200CX (JAPAN). The pulsed light of 660 nm was provided by a light-emitting diode (L3882, Hamamatsu) powered by a signal generator (33600A, KEYSIGHT). The laser of 1550 nm was obtained by MDL-N-1550-3W (Changchun, China).

THEORETICAL CALCULATIONS

Density Functional Theory Calculation. Density functional theory (DFT) calculations were conducted using the

https://doi.org/10.1021/acsami.3c13305
ACS Appl. Mater. Interfaces 2023, 15, 56526−56536

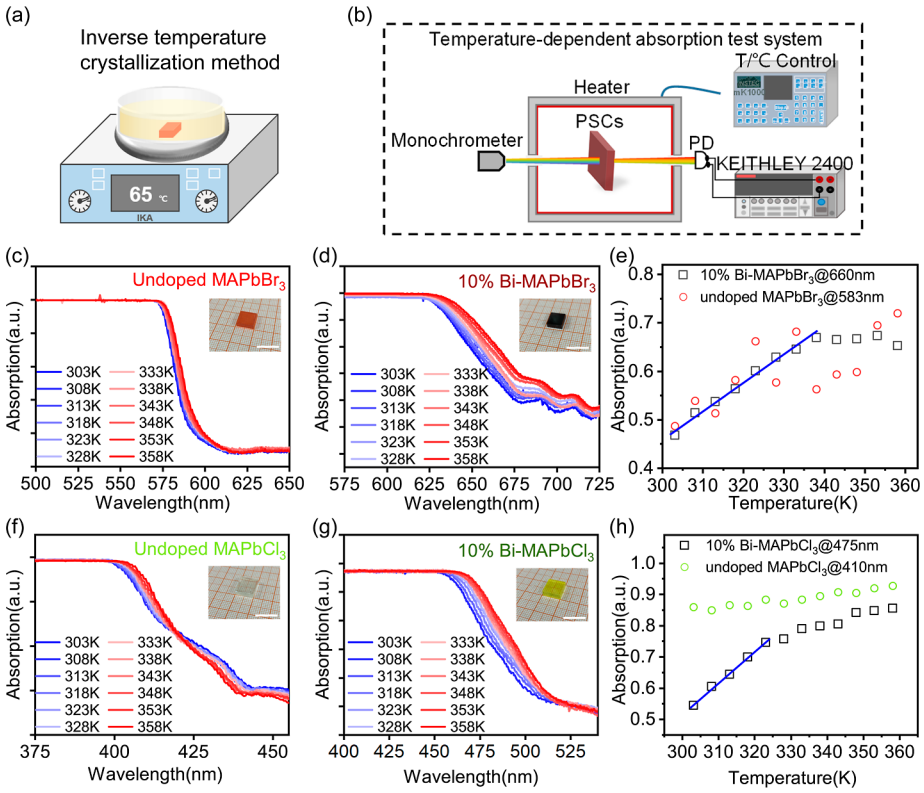

Figure 1. Temperature-dependent absorption characterization of perovskite SCs. (a) Growth process of SCs by the ITC method. (b) Schematic diagram of the temperature-dependent absorption test system. The PD is based on a silicon PIN detector. (c) Normalized absorption spectra of undoped $MAPbBr_3$ SCs at various temperatures. (d) Normalized absorption spectra of 10% Bi-$MAPbBr_3$ SCs at various temperatures. (e) Absorptivity temperature dependence for undoped $MAPbBr_3$ SCs (@583 nm) and 10% Bi-$MAPbBr_3$ SCs (@660 nm) at their most thermal sensitive wavelength. (f) Normalized absorption spectra of undoped $MAPbCl_3$ SCs at various temperatures. (g) Normalized absorption spectra of 10% Bi-$MAPbCl_3$ SCs at various temperatures. (h) Absorptivity temperature dependence for undoped $MAPbCl_3$ SCs (@410 nm) and 10% Bi-$MAPbCl_3$ SCs (@475 nm) at their most thermal sensitive wavelength.

projector-augmented wave method as implemented in the VASP code.[23] The plane-wave cutoff energy was set to 450 eV. The generalized gradient approximation (GGA) Perdew–Burke–Ernzerhof (PBE) functional and Γ-centered grid *k*-meshes with a *k*-spacing of 0.3 $Å^{-1}$ were employed for structural relaxations, which stopped when the total force on each atom was smaller than 0.03 eV/Å.

RESULTS AND DISCUSSION

According to the blackbody radiation law, objects at a temperature above absolute zero can emit IR radiation, which is an electromagnetic wave that cannot be directly seen by human eyes.[7] Therefore, the thermograph by responding to radiative IR photons shows significance in identifying the substances under the weak visible light condition, such as monitoring the battery safety, chip temperature, agricultural production,[24] and human body health,[4] as depicted in Figure S1. However, their poor integration in the established optical system imposes an impediment to their practical application due to the poor transmission of thermal energy. Thus, in this work, we will develop a sensitive and feasible thermograph by sensing the visible photons.

Doping is a common method for inducing defects or excitation in materials and shows the influence on their intrinsic properties including the optical band gap, carrier transport, or recombination.[25] The manipulation of the doping concentration was designed to form a doping level for realizing IR detection.[26] Taking the star material of lead halide perovskites as an example, it undergoes an explosive development in optoelectronic devices due to the merits in the facile solution processing fabrication and excellent optoelectronic properties.[27] The soft lattice in the perovskite also promises the lead analogous ion dopant incorporation.[28] Until now, the heterovalent dopants of Ag, Sb, Bi, Fe, Ce, Sr, etc. have been explored as dopants, in which Bi can be used as an n-type dopant and the doping concentration can be easily controlled with the experiment condition.[29] Moreover, it is revealed that the Bi substitution in the perovskite lattice can significantly modify its thermoelectric properties.[22] Thus, in this work, the Bi-$MAPbX_3$ SC is selected as the sensitive material.

Figure 1a shows the schematic diagram of solution processing fabrication for the proposed Bi-$MAPbX_3$ SCs, in which the ITC method is used.[30] To facilitate the doping of Bi into $MAPbX_3$, beyond the stoichiometric ratio between PbX_2 and MAX, extra BiX_3 was added to the precursor.

The details can be found in the Experimental Section. To identify whether the doping is beneficial for the thermography, the temperature-dependent absorption analysis in $MAPbBr_3$ and Bi-$MAPbBr_3$ was conducted. Figure 1b depicts a schematic diagram of the homemade testing system. Similar to spectrometers, this system consists of a monochromator, a photodetector, and a microcomputer for recording spectra. The heater and the precision temperature controller are essential parts in the temperature-dependent absorption test. During the measurement, the SCs are held in the sample

https://doi.org/10.1021/acsami.3c13305
ACS Appl. Mater. Interfaces 2023, 15, 56526−56536

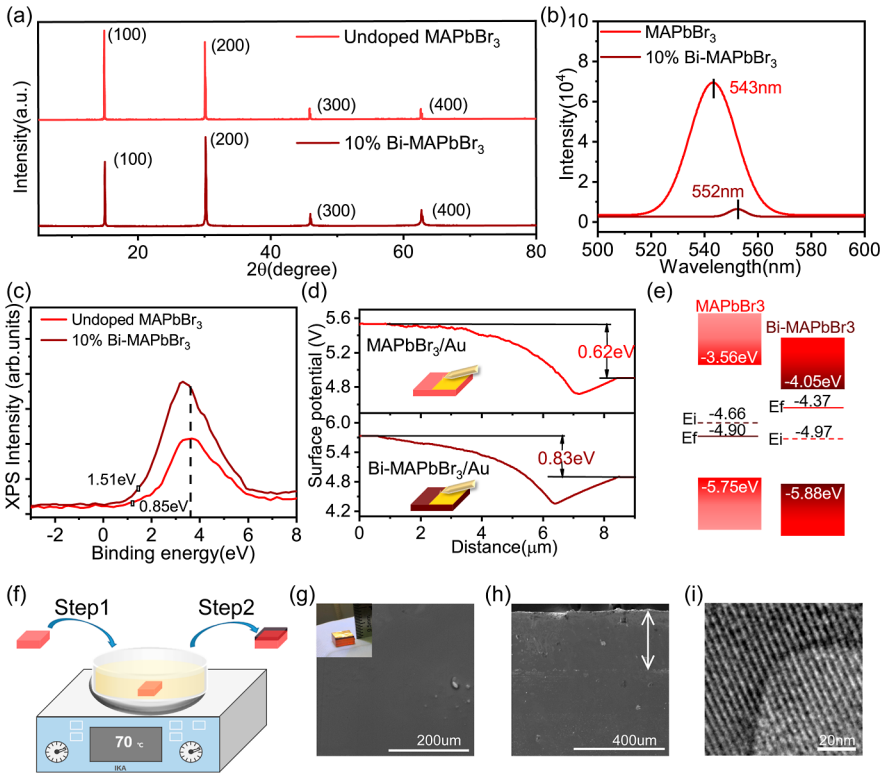

Figure 2. Basic optical properties of undoped $MAPbBr_3$, Bi-$MAPbBr_3$, and the epitaxial homostructure. (a) XRD patterns of undoped $MAPbBr_3$ SCs and 10% Bi-$MAPbBr_3$ SCs, respectively. (b) PL spectra of undoped $MAPbBr_3$ SCs and Bi-$MAPbBr_3$ SCs, respectively. (c) XPS spectra of undoped $MAPbBr_3$ SCs and 10% Bi-$MAPbBr_3$ SCs, respectively. (d) KPFM measurements of undoped and 10% Bi SCs and surface potential differences between undoped $MAPbBr_3$ SCs and gold and 10% Bi-$MAPbBr_3$ SCs and gold, respectively. (e) Band gap alignment of undoped $MAPbBr_3$ and 10% Bi-$MAPbBr_3$. (f) Schematic diagram of the SPE growth process. (g) SEM image of the surface of the epitaxial Bi-$MAPbBr_3$ layer. The scale bar is 200 μm. The inset is the picture of the $MAPbBr_3$ substrate with the epitaxial Bi-$MAPbBr_3$ layer. (h) SEM image of the cross-section of the Bi-$MAPbBr_3$ and undoped $MAPbBr_3$ homostructure. The scale bar is 400 μm. (i) HRTEM image of the interface between the substrate and epitaxial layer. The scale bar is 20 nm.

chamber with a dual top−bottom heater, which virtually eliminates vertical temperature gradients in the sample chamber. The top and bottom dual pane windows are used for visible photons going through the sample chamber. Figure 1c,d shows the normalized absorption spectra in $MAPbBr_3$ SCs and 10% Bi-$MAPbBr_3$ SCs at various temperatures. The inset shows the photograph of SCs. As expected, a significant enhancement is observed in the absorption edge with the increasing temperature.

Compared with $MAPbBr_3$ SCs, 10% Bi-$MAPbBr_3$ SCs possess a clear red shift in absorption, and the energy of the photon is even beyond the optical band gap. This result further verifies that the Bi ions incorporation forms the interband, which is essential for low-energy IR photon detection or constructing the thermograph. More importantly, the variation of visible photon absorption along with the change in the temperature also lays a foundation for realizing sensitive thermography. To magnify this thermal sensitivity, Figure 1e presents the absorption toward the characteristic photons of 660 and 583 nm in Bi-$MAPbBr_3$ and $MAPbBr_3$ SCs, respectively.

Although both Bi-$MAPbBr_3$ and $MAPbBr_3$ present the obvious change, only the absorption in Bi-$MAPbBr_3$ shows a linear variation and the linear dynamic region ranges from 303 to 343 K. Notably, this linear variation is important in enabling the high thermal resolution in temperature detection, which confirms the potential of Bi-$MAPbBr_3$ for constructing the sensitive thermograph. Figure 1f,g shows normalized absorption spectra in $MAPbCl_3$ SCs and 10% Bi-$MAPbCl_3$ SCs at various temperatures. The linear variation of absorption on temperature was also found in Bi-$MAPbCl_3$ SCs from 303 to 323 K (Figure 1h).

As we demonstrate above, the incorporation of Bi in $MAPbX_3$ shows temperature-sensitive absorption. Taking the as-fabricated $MAPbBr_3$ with 10% doping concentration as an example, Figure 2a gives its XRD profile. Figure S2 presents the absorption of Bi-$MAPbBr_3$ at different doping concentrations. Notably, herein, the doping concentration is the molar ratio of BiX_3 in the precursor. To provide a visual comparison, the data of the intrinsic $MAPbBr_3$ are presented. As we can see, both $MAPbBr_3$ and Bi-$MAPbBr_3$ SCs exhibit the pure cubic phase and high crystal crystallinity. Due to the similar ionic radii of Bi^{3+} (1.03 Å) and Pb^{2+}(1.19 Å), the characteristic peaks indicate a negligible change in the lattice. Similar to $MAPbBr_3$, the Bi ion can also be doped into $MAPbCl_3$, and their XRD pattern can be found in Figure S3. Figure 2b displays the PL spectra in $MAPbBr_3$ and Bi-$MAPbBr_3$. The incorporation of Bi not only reduces the PL intensity but also shifts the PL peak from 543 to 552 nm. This result indicates that Bi doping can narrow the optical band gap of $MAPbBr_3$ and enhance the nonradiative recombination.[31] Additionally, Figure S4 shows the PL spectra of undoped $MAPbCl_3$ SCs and Bi-$MAPbCl_3$ SCs. Figure S5 shows the major carrier concentration in Bi-$MAPbBr_3$, $MAPbBr_3$ and Bi-$MAPbCl_3$,

https://doi.org/10.1021/acsami.3c13305
ACS Appl. Mater. Interfaces 2023, 15, 56526−56536

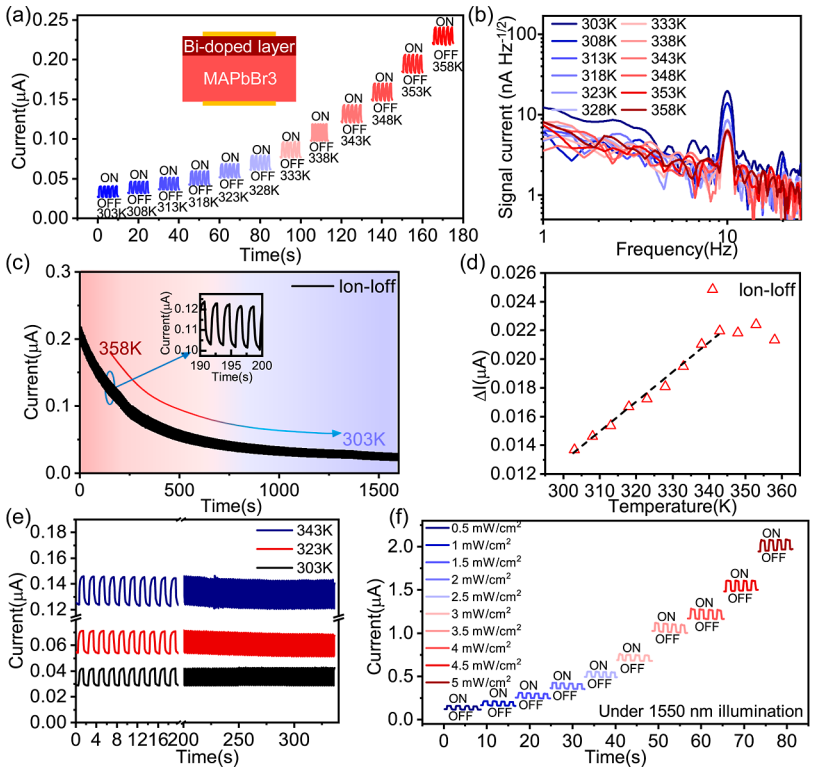

Figure 3. Thermal response properties of the device based on the epitaxial Bi-MAPbBr$_3$ layer. (a) Photocurrents at 660 nm of the device based on Au/Bi-MAPbBr$_3$/undoped MAPbBr$_3$/Au at different temperatures. (b) Signal-to-noise currents measured by the FFT of the device with Bi-MAPbBr$_3$ layers under −10 V. (c) Difference between I_{ON} and I_{OFF} of the device at different temperatures. (d) Photocurrents at 660 nm of the device with the temperature decreasing from 358 to 303 K. (e) Long-term temperature-sensitive response stability of the device. (f) Temporal photoresponse at 660 nm of device A under 1550 nm IR illumination with different intensities.

MAPbCl$_3$ from the Hall effect measurement.[28,29] The incorporation of Bi^{3+} ions can change the majority carrier from holes to electrons and significantly increase their concentration. Figure 2e displays the energy level in MAPbBr$_3$ and Bi-MAPbBr$_3$, in which the differences between the Fermi level (E_F) and the valence band maximum (E_{VBM}) were estimated from XPS results (Figure 2c), and the E_F is extracted from KPFM (Figure 2d).[32] The differences of E_F and E_{VBM} were measured to be 1.5 and 0.85 eV for Bi-MAPbBr$_3$ SCs and undoped MAPbBr$_3$ SCs, respectively, and the Fermi levels of undoped MAPbBr$_3$ SCs and Bi-MAPbBr$_3$ SCs are 0.62 and 0.83 eV higher than that of gold, respectively.

Bi doping enhances the carrier recombination, as well as temperature-sensitive absorption of MAPbBr$_3$. In this case, a p−n junction with homoepitaxial Bi-MAPbBr$_3$ layers (n-type) on MAPbBr$_3$ SC (p-type) substrates was designed to optimize the carrier dynamics. Figure 2f shows the two steps of the SPE growth process of homoepitaxial Bi-MAPbBr$_3$ layers. Step 1: the MAPbBr$_3$ SC structure was placed into the Bi-MAPbBr$_3$ precursor solution. Step 2: the extra area was cut off, and the surface was polished. Figure 2g presents its top-view SEM image, in which the Bi-MAPbBr$_3$ layer shows a smooth and compact surface. The intact surface proves that the Bi-MAPbBr$_3$ SC is of high quality. It is important to improve the device performance since the published studies indicated that the carrier recombination mainly occurs at the crystal domain surface.[33,34] The inset in Figure 2g displays the photograph of the as-fabricated thermograph with Bi-MAPbBr$_3$/MAPbBr$_3$ SCs and Au electrodes. As we can observe, the visual color at the interface changes from orange in MAPbBr$_3$ to dark brown in Bi-MAPbBr$_3$. Figure 2h provides the cross-section SEM image. It identifies the thicknesses in Bi-MAPbBr$_3$ and MAPbBr$_3$ layers as 267 μm and 3 mm, respectively. The thin thickness in Bi-MAPbBr$_3$ enables the built-in potential to drive its thermal energy generated carriers to the external circuit. The energy-dispersive X-ray spectroscopy (EDX) spectra of the Bi elements in devices are shown in Figure S6. A clear emergence of the Bi element appears in the Bi-MAPbBr$_3$ SC layer.

Meanwhile, the HRTEM image (Figure 2i) reveals a well-aligned cubic lattice between epitaxial layers without dislocations.[33] This result verifies that the Bi doping will not change the lattice parameters, which coincides with the XRD result. Moreover, the perfect lattice match ensures charge carrier transport at the interface between Bi-MAPbBr$_3$ and MAPbBr$_3$ layers.[35]

Similar to the measurement of temperature-sensitive absorption, a pulsed light at 660 nm (the most absorption-sensitive wavelength) with a modulated on/off switch frequency of 0.5 Hz (10 Hz) was employed. Figure 3a depicts the photoresponse toward 660 nm photons in our thermograph at a −10 V bias under various temperatures.

The temperature of the sample chamber increased from 303 to 358 K with an interval of 5 K. As shown, the dark currents increase with the temperature due the bolometric effect in the perovskite, as revealed in our previous work.[18] Even so, the photocurrents display an obvious enhancement under 660 nm illumination. To prove the feature that the differences between I_{ON} and I_{OFF} increase linearly with temperature is caused by epitaxial Bi-doped layers, we tested the photocurrents of

https://doi.org/10.1021/acsami.3c13305
ACS Appl. Mater. Interfaces 2023, 15, 56526−56536

Table 1. Comparison of Typical IR Thermal Detectors

device structure	responsivity	D^*(Jones)	sensitivity (%/K)	reference
a-Si_xGe_y/H	2×10^{-3} A/W	7×10^{9}	0.043	39
V_2O_5	36 V/W	6×10^{5}	2.8	40
poly-SiGe	15,000 V/W	8.3×10^{8}	−1.91	41
metal multiwalled carbon nanotube	0.503 V/W		−0.11	42
PV/CaF_2/NiCr/HgTe QD/Ag @290 K	1×10^{-3} A/W	1.2×10^{7}		43
PV/ITO/HgTeQD/Ag_2Te QD/$HgCl_2$/Au @295 K	8×10^{-2} A/W	3×10^{8}		14
PbSe @4 μm	0.64 A/W	8.36×10^{8}		44
PbSe/CdSe @4.2 μm	7.5×10^{-2} A/W	1.02×10^{9}		45
Au/Bi-$MAPbBr_3$/undoped $MAPbBr_3$/Au	2.06×10^{-3} A/W	2.08×10^{9}	2.11	this work

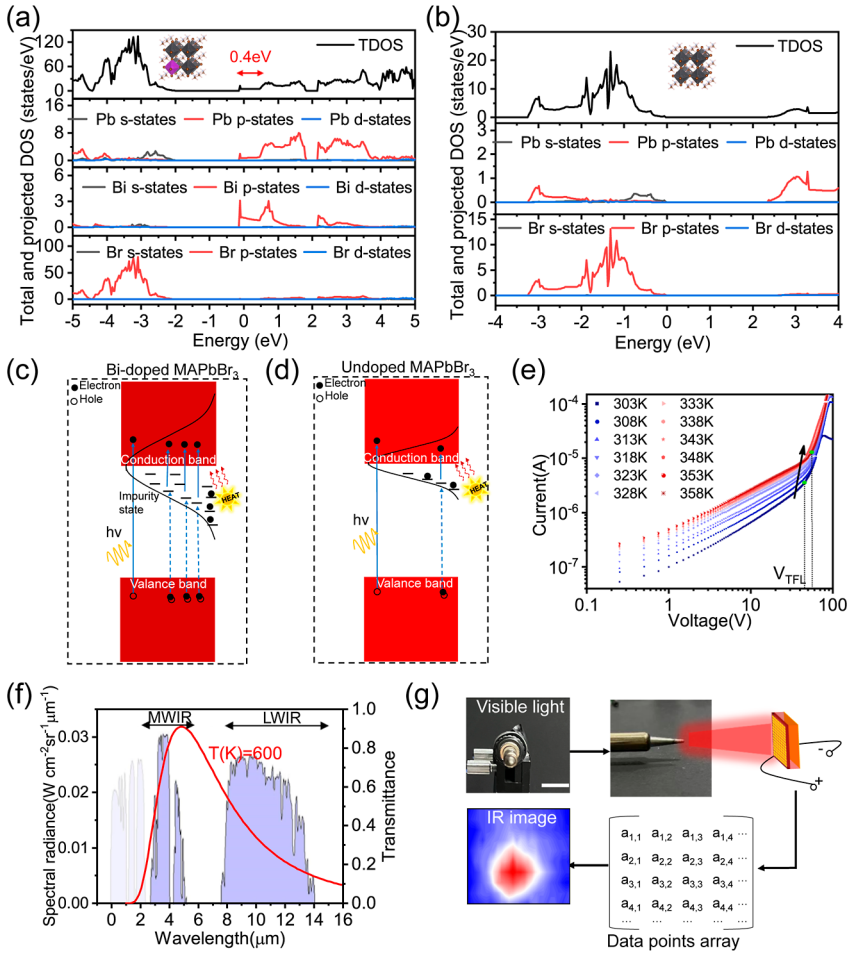

Figure 4. Schematic diagram of the device with the Bi-doping-induced trap state in $MAPbX_3$. Total and projected DOS diagrams of (a) undoped $MAPbBr_3$ and (b) $MAPbBr_3$ with 10% Bi doping. (c,d) Proposed charge carrier excitation process of Bi-$MAPbBr_3$ and undoped $MAPbBr_3$, respectively. (e) Trap density measured by the space-charge-limited-current (SCLC) method at various temperatures. Application of the device for IR thermal imaging. (f) Electromagnetic radiation emitted by a soldering iron tip at 600 K. (g) Schematic diagram of the IR thermal imaging setup.

detectors based on Au/undoped $MAPbBr_3$/Au at various temperatures for comparison, as depicted in Figure S7. There is no obviously enhancement for the photocurrents of the device based only on undoped $MAPbBr_3$ SCs under 583 nm illumination. Figure 3b illustrates the signal-to-noise ratio measured by the fast Fourier transform (FFT) under 660 nm photon illumination with a modulation frequency of 10 Hz at various temperatures. Clearly, the photocurrents signal peak gradually decreases with the temperature from 19.71 nA $Hz^{-1/2}$ at 303 K to 6.27 nA $Hz^{-1/2}$ at 358 K.[36] It confirms the temperature-sensitive electric signal in our thermograph originating from the response of 660 nm photon irradiation.

To extract the precise influence of temperature on photocurrent, the differences between photocurrents (I_{ON}) and dark currents (I_{OFF}) under various temperatures are obtained. It is clearly shown in Figure 3c that the differences between I_{ON} and I_{OFF} increase linearly with temperature from 303 to 343 K, and a saturation emerges at temperatures over 343 K. This phenomenon is the same as that in temperature-sensitive absorption. It is reasonable to ascribe the variation in the differences between I_{ON} and I_{OFF} to the change in the 660 nm photon absorption. Figure 3d displays the differences between I_{ON} and I_{OFF} with temperature continuously decreasing from 358 to 303 K. Figure S8 gives the variation of the photocurrent

https://doi.org/10.1021/acsami.3c13305
ACS Appl. Mater. Interfaces 2023, 15, 56526−56536

difference as the temperature decreases. Especially, during the cooling, the photocurrent difference still presents a linear dependence on temperature, which proves the excellent repeatability of our thermograph. To quantify the temperature sensitivity of our devices, we defined the thermal response current coefficient as

$$k \equiv \frac{\partial(I_{ON} - I_{OFF})}{(I_{ON} - I_{OFF})\partial T} \quad (2)$$

The sensitivity in our device is estimated to be 2.11% K^{-1}, which is several orders of magnitude larger than that for the temperature coefficient of resistance (TCR) of typical resistance thermometers.[37] Moreover, our devices have a high temperature resolution of 0.21 nA K^{-1} in the linear dynamic range. Figure 3e shows the long-term temporal response in our thermograph toward pulsed 660 nm photons with the power of 2.5 mW cm^{-2} under various temperatures. Also, no change in the baseline or photoresponse is observed, which indicates a good temperature tolerance and good repeatability. It is essential to ensure the temperature resolution in thermography.

In general, the requirement in practical applications for thermographs is the capacity for remote sensing. To check the potential of our device for noncontact real-time thermography, the 1550 nm photon is adopted to simulate the thermal radiation. Figure 3f shows the temporal response of our thermograph to 660 nm photons under 1550 nm irradiation with different intensities. Our device absorbs the IR photon and converts it into thermal energy, which subsequently affects the photocurrent resulting from 660 nm photon irradiation. Thus, the photocurrent difference increases as the IR intensity increases. To better describe this performance, the responsivity (R) and detectivity (D^*) were calculated from the photocurrents. R is defined as

$$R = \frac{I_{ON} - I_{OFF}}{P_{light} \times S} \quad (3)$$

where S is the effective area and P_{light} is the light intensity. D^* is simplified as

$$D^* = R\sqrt{\left(\frac{s}{2qI_{OFF}}\right)} \quad (4)$$

in which q is the electron charge (1.6×10^{-19} C).[38] Figure S9 gives the calculated R and D^* at different intensities. The highest R and D^* in our thermograph under 0.5 mW cm^{-2} of 1550 nm illumination were calculated to be 2.06 mA W^{-1} and 2.08×10^9 Jones, respectively. To better understand the advances, Table 1 gives the comparison of the performance between our thermograph and the typical IR thermal detectors.

The importance of Bi incorporation is underscored by the results from temperature-sensitive absorption and visible photon detection. To further clarify the role of Bi doping, we next investigate the density of states (DOS) in Bi-$MAPbBr_3$ and $MAPbBr_3$ with the assistance of DFT calculation.[23] Figure 4a,b presents the calculation result. Due to the characteristics of the electron donor, Bi ions make a significant contribution to the DOS. As we can see, the incorporation of Bi ions brings a non-negligible trap state distribution in the forbidden band, and the edge of the addition state is ~0.4 eV to the conduction band maximum (CBM) of $MAPbBr_3$. It is worth noting that the distribution of extra states is continuous and extends to the CBM. To better understand the effect of Bi doping on the temperature-sensitive absorption, Figure 4c,d shows the proposed charge carrier excitation process. The additional trap states enable the acceptance of carriers pumped by the absorption of visible photons with energy lower than the band gap. The overlap between trap states and the conduction band in Bi-$MAPbBr_3$ facilitates some trapped charge carriers jumping to the conduction band under thermal energy excitation. The left trap state is empty, and it enhances the subsequent absorption (Figure 3a). This dynamic process results in temperature-sensitive absorption. To corroborate this process, the trap density (n_{traps}) under various temperatures was estimated using the SCLC method, as shown in Figure 4e. The formula is

$$n_{traps} = \frac{2\varepsilon V_{TFL}}{qL^2} \quad (5)$$

where ε is relative dielectric constant, V_{TFL} is the trap-filled limit voltage at which all injected charge carriers are used to fill all traps, q is the electronic charge, and L is the distance between the opposite electrodes.[46] As expected, with the temperature increasing from 303 to 358 K, the V_{TFL} increases from 45.5 to 56.0 V, leading to the calculated n_{traps} increasing from 2.85×10^{11} cm^{-3} to 3.51×10^{11} cm^{-3}. Obviously, the trap/detrap processing in the additional states originating from Bi doping plays an indispensable role in realizing this temperature-sensitive functionality.

To further verify the potential of our thermograph in practical application, the noncontact real-time thermal imaging was conducted with an electric soldering iron tip as the sensing target. Under work conditions, the temperature on the electric soldering iron tip approaches 600 K. According to the blackbody radiation law, its radiation wavelength can be calculated with the following equation

$$u_v(\nu,T) = \frac{8\pi h\nu^3}{c^3}\frac{1}{\frac{h\nu}{e^{KT-1}}} \quad (6)$$

in which h is the Planck constant, ν is the frequency, c is the speed of light, and k are T are the Boltzmann constant and temperature, respectively.[10] As shown in Figure 4f, the wavelength of IR radiation from the soldering iron tip mainly localizes in the atmospheric window (3−5 and 8−13 μm),[11] which endows the remote thermal imaging. Figure 4g illustrates the schematic diagram of a homemade thermal imaging setup, in which the distance between our thermograph and the electric soldering iron tip is ~30 cm.

Clearly, the obtained patterns perfectly reflect the temperature distribution around the electric soldering iron tip. The gradient change in the imaging also further identifies the advantage of high temperature resolution in our thermograph. According to the practical condition for thermal imaging of the soldering iron tip, in which the thermal energy density on each pixel is $\sim 8.2 \times 10^{-2}$ W m^{-2}, it is reasonable to deduce that even without the assistance of an optical system, our thermograph can be used as a noncontact thermometer.

CONCLUSIONS

As conclusions, we discovered that the Bi-$MAPbX_3$ SCs have a linear temperature dependence of absorption due to the trap states induced by Bi dopants. According to these temperature-induced changes in the absorption, we fabricated a thermo-

https://doi.org/10.1021/acsami.3c13305
ACS Appl. Mater. Interfaces 2023, 15, 56526−56536

graph with p−n junctions based on the homoepitaxial Bi-$MAPbBr_3$ (n-type) on the intrinsic $MAPbBr_3$ (p-type) substrates. The differences between I_{ON} and I_{OFF} by sensing visible photons is successfully applied to characterize the temperature and thermal imaging, in which a high responsivity of 2.06 mA W^{-1}, a high detectivity of 2.08×10^9 Jones, and a high sensitivity of 2.11% K^{-1} are achieved. We believe that the detection of visible photons in our thermograph will enable its integration with the conventional optical system for imaging with high spatial resolution and thermal resolution.

■ ASSOCIATED CONTENT

Supporting Information

The Supporting Information is available free of charge at https://pubs.acs.org/doi/10.1021/acsami.3c13305.

The absorption of Bi-$MAPbBr_3$ with different doping concentrations; XRD patterns of undoped $MAPbCl_3$ and Bi-$MAPbCl_3$, respectively; Hall effect of undoped and 10% Bi-doped SCs to measure the majority carrier density and type; EDX results for SC devices with epitaxial Bi-doped layers; the variation of the photocurrent difference with the decrease in the temperature; and calculated responsivity (R) and detectivity (D^*) of the device (PDF)

■ AUTHOR INFORMATION

Corresponding Authors

Wei Lei − *School of Electronic Science and Engineering Joint International Research Laboratory of Information Display and Visualization, Southeast University, Nanjing 210000, China*; Email: lw@seu.edu.cn

Xiaobao Xu − *School of Electronic Science and Engineering Joint International Research Laboratory of Information Display and Visualization, Southeast University, Nanjing 210000, China*; orcid.org/0000-0001-5378-5604; Email: xiaobaoxu@njust.edu.cn

Authors

Yubing Xu − *School of Electronic Science and Engineering Joint International Research Laboratory of Information Display and Visualization, Southeast University, Nanjing 210000, China*

Xin Wang − *School of Electronic Science and Engineering Joint International Research Laboratory of Information Display and Visualization, Southeast University, Nanjing 210000, China*

Shilin Liu − *School of Electronic Science and Engineering Joint International Research Laboratory of Information Display and Visualization, Southeast University, Nanjing 210000, China*

Yuzhu Pan − *School of Electronic Science and Engineering Joint International Research Laboratory of Information Display and Visualization, Southeast University, Nanjing 210000, China*; orcid.org/0000-0002-0685-2840

Abida Perveen − *School of Electronic Science and Engineering Joint International Research Laboratory of Information Display and Visualization, Southeast University, Nanjing 210000, China*

Damian Chinedu Onwudiwe − *Department of Chemistry, School of Mathematics and Physical Sciences Faculty of Natural and Agricultural Sciences, North-West University, Mafikeng Campus, Mmabatho 2735, South Africa*

Omolola Esther Fayemi − *Department of Chemistry, School of Mathematics and Physical Sciences Faculty of Natural and Agricultural Sciences, North-West University, Mafikeng Campus, Mmabatho 2735, South Africa*; orcid.org/0000-0002-0049-5184

Elias Emeka Elemike − *Department of Chemistry, School of Mathematics and Physical Sciences Faculty of Natural and Agricultural Sciences, North-West University, Mafikeng Campus, Mmabatho 2735, South Africa*

Byung Seong Bae − *Department of Electronics & Display Engineering, Hoseo University, Asan city, Chungnam 31499, Republic of Korea*; orcid.org/0000-0002-3328-0286

Ying Zhu − *E-xray Electronic Co. Ltd., Suzhou 215000, China*

Razika Zair Talaighil − *Institute of Electrical & Electronic Engineering, M'hamed Bougara University of Boumerdes, Boumerdes 35000, Algeria*

Xiaobing Zhang − *School of Electronic Science and Engineering Joint International Research Laboratory of Information Display and Visualization, Southeast University, Nanjing 210000, China*

Jing Chen − *School of Electronic Science and Engineering Joint International Research Laboratory of Information Display and Visualization, Southeast University, Nanjing 210000, China*; orcid.org/0000-0001-6703-2486

Zhiwei Zhao − *School of Electronic Science and Engineering Joint International Research Laboratory of Information Display and Visualization, Southeast University, Nanjing 210000, China*

Qing Li − *School of Electronic Science and Engineering Joint International Research Laboratory of Information Display and Visualization, Southeast University, Nanjing 210000, China*

Complete contact information is available at: https://pubs.acs.org/10.1021/acsami.3c13305

Author Contributions

Y.X. and Y.P. grew the perovskite single crystals. Y.X. and X.W. conducted the epitaxial experiments. Y.X. and X.W. obtained the measurements. L.S. performed the DFT calculations. Y.X., X.W., W.L., and X.X. analyzed these results. The manuscript was written through contributions of all authors. All authors have given approval to the final version of the manuscript.

Notes

The authors declare no competing financial interest.

■ ACKNOWLEDGMENTS

This work was financially supported by the National Key Research and Development Program of China (2021YFE0105900 and 2022YFE0139100), National Natural Science Foundation Project of China (62175028, 51879042, 61674029, and 12375306), National Natural Science Foundation Project for Young Researcher (12005038), Program 111_2.0 in China (BP0719013), Leading Technology of Jiangsu Basic Research Plan (BK20192003), International cooperative research project of Jiangsu province (BZ2022008), and Basic Research Program of Jiangsu Province (BK20212006).

■ ABBREVIATIONS

MA, methylammonium; IR, infrared; SCs, single crystals; XRD, X-ray diffraction; PL, photoluminescence; ITC, inverse temperature crystallization; SEM, scanning electron micros-

copy; HRTEM, high-resolution transmission electron microscopy; FFT, fast Fourier transform; EDX, energy-dispersive X-ray spectroscopy; KPFM, Kelvin probe force microscopy; TCR, temperature coefficient of resistance; DFT, density functional theory; CBM, conduction band maximum; SCLC, space-charge-limited-current

REFERENCES

(1) Yakunin, S.; Benin, B. M.; Shynkarenko, Y.; Nazarenko, O.; Bodnarchuk, M. I.; Dirin, D. N.; Hofer, C.; Cattaneo, S.; Kovalenko, M. V. High-resolution Remote Thermometry and Thermography using Luminescent Low-dimensional Tin-halide Perovskites. *Nat. Mater.* **2019**, *18* (8), 846−852.

(2) Yadav, P. K.; Yadav, I.; Ajitha, B.; Rajasekar, A.; Gupta, S.; Ashok Kumar Reddy, Y. Advancements of Uncooled Infrared Microbolometer Materials: A Review. *Sens. Actuators, A* **2022**, *342*, 113611.

(3) Gonzalez, A.; Fang, Z.; Socarras, Y.; Serrat, J.; Vazquez, D.; Xu, J.; Lopez, A. M. Pedestrian Detection at Day/Night Time with Visible and FIR Cameras: A Comparison. *Sensors (Basel)* **2016**, *16* (6), 820.

(4) Lahiri, B. B.; Bagavathiappan, S.; Jayakumar, T.; Philip, J. Medical Applications of Infrared Thermography: A review. *Infrared Phys. Technol.* **2012**, *55* (4), 221−235.

(5) Hong, S.; Dechaumphai, E.; Green, C. R.; Lal, R.; Murphy, A. N.; Metallo, C. M.; Chen, R. Sub-nanowatt Microfluidic Single-cell Calorimetry. *Nat. Commun.* **2020**, *11* (1), 2982.

(6) (a) Menges, F.; Mensch, P.; Schmid, H.; Riel, H.; Stemmer, A.; Gotsmann, B. Temperature Mapping of Operating Nanoscale Devices by Scanning Probe Thermometry. *Nat. Commun.* **2016**, *7*, 10874. (b) Halbertal, D.; Cuppens, J.; Shalom, M. B.; Embon, L.; Shadmi, N.; Anahory, Y.; Naren, H. R.; Sarkar, J.; Uri, A.; Ronen, Y.; et al. Nanoscale Thermal Imaging of Dissipation in Quantum Systems. *Nature* **2016**, *539* (7629), 407−410.

(7) Bagavathiappan, S.; Lahiri, B. B.; Saravanan, T.; Philip, J.; Jayakumar, T. Infrared Thermography for Condition Monitoring - A Review. *Infrared Phys. Technol.* **2013**, *60*, 35−55.

(8) Zhang, F.; Zang, Y.; Huang, D.; Di, C. A.; Zhu, D. Flexible and Self-powered Temperature- Pressure Dual-parameter Sensors using Microstructure-frame-supported Organic Thermoelectric Materials. *Nat. Commun.* **2015**, *6*, 8356.

(9) Wei, Z.; Wang, L.; Guo, W. Secret Key Rate Upper-bound for Reconfigurable Intelligent Surface-combined System under Spoofing. In *2022 IEEE 96th Vehicular Technology Conference (VTC2022-Fall)*, 2022.

(10) García-García, A. M. Finite-size Corrections to the Blackbody Radiation Laws. *Phys. Rev. A* **2008**, *78* (2), 023806.

(11) Usamentiaga, R.; Venegas, P.; Guerediaga, J.; Vega, L.; Molleda, J.; Bulnes, F. G. Infrared Thermography for Temperature Measurement and Non-destructive Testing. *Sensors (Basel)* **2014**, *14* (7), 12305−12348.

(12) (a) Zhao, Y.; Tang, L.; Yang, S.; Lau, S. P.; Teng, K. S. Infrared Photovoltaic Detector based on p-GeTe/n-Si Heterojunction. *Nanoscale Res. Lett.* **2020**, *15* (1), 138. (b) Huang, L.; Chen, J.; Yu, Z.; Tang, D. Self-Powered Temperature Sensor with Seebeck Effect Transduction for Photothermal-Thermoelectric Coupled Immunoassay. *Anal. Chem.* **2020**, *92* (3), 2809−2814. (c) Jiang, W.; Zheng, T.; Wu, B.; Jiao, H.; Wang, X.; Chen, Y.; Zhang, X.; Peng, M.; Wang, H.; Lin, T.; et al. A Versatile Photodetector Assisted by Photovoltaic and Bolometric Effects. *Light: Sci. Appl.* **2020**, *9*, 160.

(13) (a) Schaefer, S. T.; Gao, S.; Webster, P. T.; Kosireddy, R. R.; Johnson, S. R. Absorption Edge Characteristics of GaAs, GaSb, InAs, and InSb. *J. Appl. Phys.* **2020**, *127* (16), 165705. (b) Lautenschlager, P.; Garriga, M.; Logothetidis, S.; Cardona, M. Interband Critical Points of GaAs and Their Temperature Dependence. *Phys. Rev. B: Condens. Matter Mater. Phys.* **1987**, *35* (17), 9174−9189. (c) Xue, X.; Chen, M.; Luo, Y.; Qin, T.; Tang, X.; Hao, Q. High-operating-temperature Mid-infrared Photodetectors via Quantum Dot Gradient Homojunction. *Light: Sci. Appl.* **2023**, *12* (1), 2.

(14) Ackerman, M. M.; Tang, X.; Guyot-Sionnest, P. Fast and Sensitive Colloidal Quantum Dot Mid-Wave Infrared Photodetectors. *ACS Nano* **2018**, *12* (7), 7264−7271.

(15) (a) Kang, D.; Kim, H. S.; Han, S.; Lee, Y.; Kim, Y. P.; Lee, D. Y.; Lee, J. A Local Water Molecular-heating Strategy for Near-infrared Long-lifetime Imaging-guided Photothermal Therapy of Glioblastoma. *Nat. Commun.* **2023**, *14* (1), 2755. (b) Wang, Q.; Wu, Y.; Deng, X.; Xiang, L.; Xu, K.; Li, Y.; Xie, Y. Preparation and Bolometric Responses of MoS(2) Nanoflowers and Multi-Walled Carbon Nanotube Composite Network. *Nanomaterials (Basel)* **2022**, *12* (3), 495. (c) Degardin, A. F.; Jagtap, V. S.; Razanoelina, M.; Galiano, X.; Tonouchi, M.; Kreisler, A. J.; Salmon, N. A.; Gumbmann, F. Y-Ba-Cu-O Semiconducting Pyroelectric Thermal Sensors: Design and Test of Near-infrared Amorphous Thin Film Detectors and Extension to Antenna-coupled THz Devices. *Millimetre Wave and Terahertz Sensors and Technology XII*, 2019. (d) Lin, S.; Yan, L.; Zhao, L.; Cai, Z.; Liu, Z.; Yang, B.; Yang, M.; Zhao, C. Strain Engineering for Tailored Carrier Transport and Thermoelectric Performance in Mixed Halide Perovskites CsPb(I1-xBrx)3. *ACS Appl. Energy Mater.* **2021**, *4* (12), 14508−14519. (e) Haque, M. A.; Kee, S.; Villalva, D. R.; Ong, W. L.; Baran, D. Halide Perovskites: Thermal Transport and Prospects for Thermoelectricity. *Adv. Sci. (Weinheim, Ger.)* **2020**, *7* (10), 1903389.

(16) Jiang, Y.; Dong, J.; Zhuang, H. L.; Yu, J.; Su, B.; Li, H.; Pei, J.; Sun, F. H.; Zhou, M.; Hu, H.; et al. Evolution of Defect Structures Leading to High ZT in GeTe-based Thermoelectric Materials. *Nat. Commun.* **2022**, *13* (1), 6087.

(17) Reihani, A.; Meyhofer, E.; Reddy, P. Nanokelvin-resolution Thermometry with a Photonic Microscale Sensor at Room Temperature. *Nat. Photonics* **2022**, *16* (6), 422−427.

(18) Li, J.; Zou, Y.; Hu, D.; Gu, Y.; Han, Z.; Liu, J.; Xu, X. Enhanced Room-temperature Terahertz Detection and Imaging Derived from Anti-reflection 2D Perovskite Layer on MAPbI(3) Single Crystals. *Nanoscale* **2022**, *14* (16), 6109−6117.

(19) Allison, S. W.; Gillies, G. T. Remote Thermometry with Thermographic Phosphors: Instrumentation and Applications. *Rev. Sci. Instrum.* **1997**, *68* (7), 2615−2650.

(20) Neumann, P.; Jakobi, I.; Dolde, F.; Burk, C.; Reuter, R.; Waldherr, G.; Honert, J.; Wolf, T.; Brunner, A.; Shim, J. H.; et al. High-precision Nanoscale Temperature Sensing using Single Defects in Diamond. *Nano Lett.* **2013**, *13* (6), 2738−2742.

(21) (a) Aziz, A.; Aldaghfag, S. A.; Zahid, M.; Iqbal, J.; Muhammad Yaseen, M.; Somaily, H. H. Theoretical Investigation of X_2NaIO_6 (X= Pb,Sr) Double Perovskites for Thermoelectric and Optoelectronic Applications. *Phys. B* **2022**, *630*, 413694. (b) Radja, K.; Lamia Farah, B.; Ibrahim, A.; Lamia, D.; Fatima, I.; Nabil, B.; Mohamed, A.; Al-Douri, Y.; Abd El-Rehim, A. F. Investigation of Structural, Magneto-electronic, Elastic, Mechanical and Thermoelectric Properties of Novel Lead-free Halide Double Perovskite Cs2AgFeCl6: First-principles Calcuations. *J. Phys. Chem. Solids* **2022**, *167*, 110795.

(22) Tang, W.; Zhang, J.; Ratnasingham, S.; Liscio, F.; Chen, K.; Liu, T.; Wan, K.; Galindez, E. S.; Bilotti, E.; Reece, M.; et al. Substitutional Doping of Hybrid Organic-inorganic Perovskite Crystals for Thermoelectrics. *J. Mater. Chem. A* **2020**, *8* (27), 13594−13599.

(23) (a) Navas, J.; Sanchez-Coronilla, A.; Gallardo, J. J.; Cruz Hernández, N.; Pinero, J. C.; Alcantara, R.; Fernandez-Lorenzo, C.; De los Santos, D. M.; Aguilar, T.; Martin-Calleja, J. New Insights into Organic-inorganic Hybrid Perovskite CH(3)NH(3)PbI(3) Nanoparticles. An Experimental and Theoretical Study of Doping in Pb(2)(+) Sites with Sn(2)(+), Sr(2)(+), Cd(2)(+) and Ca(2)(+). *Nanoscale* **2015**, *7* (14), 6216−6229. (b) Yu, Z. L.; Zhao, Y. Q.; Wan, Q.; Liu, B.; Yang, J. L.; Cai, M. Q. Theoretical Study on the Effect of the Optical Properties and Electronic Structure for the Bi-doped CsPbBr(3). *J. Phys.: Condens. Matter* **2020**, *32* (20), 205504.

(24) Barkla, B. J.; Rhodes, T. Use of Infrared Thermography for Monitoring Crassulacean Acid Metabolism. *Funct. Plant Biol.* **2017**, *44* (1), 46−51.

(25) (a) Abdi-Jalebi, M.; Pazoki, M.; Philippe, B.; Dar, M. I.; Alsari, M.; Sadhanala, A.; Divitini, G.; Imani, R.; Lilliu, S.; Kullgren, J.; et al. Dedoping of Lead Halide Perovskites Incorporating Monovalent

https://doi.org/10.1021/acsami.3c13305
ACS Appl. Mater. Interfaces 2023, 15, 56526−56536

Cations. *ACS Nano* **2018**, *12* (7), 7301−7311. (b) Haque, M. A.; Rosas Villalva, D.; Hernandez, L. H.; Tounesi, R.; Jang, S.; Baran, D. Role of Dopants in Organic and Halide Perovskite Energy Conversion Devices. *Chem. Mater.* **2021**, *33* (21), 8147−8172. (c) Abdelhady, A. L.; Saidaminov, M. I.; Murali, B.; Adinolfi, V.; Voznyy, O.; Katsiev, K.; Alarousu, E.; Comin, R.; Dursun, I.; Sinatra, L.; et al. Heterovalent Dopant Incorporation for Bandgap and Type Engineering of Perovskite Crystals. *J. Phys. Chem. Lett.* **2016**, *7* (2), 295−301. (d) Euvrard, J.; Yan, Y.; Mitzi, D. B. Electrical Doping in Halide Perovskites. *Nat. Rev. Mater.* **2021**, *6* (6), 531−549.

(26) (a) Xu, J.; Gulzar, A.; Yang, P.; Bi, H.; Yang, D.; Gai, S.; He, F.; Lin, J.; Xing, B.; Jin, D. Recent Advances in Near-infrared Emitting Lanthanide-doped Nanoconstructs: Mechanism, Design and Application for Bioimaging. *Coord. Chem. Rev.* **2019**, *381*, 104−134. (b) Yu, X.; Zhang, S.; Zeng, H.; Wang, Q. J. Lateral Black Phosphorene P-N Junctions Formed via Chemical Doping for High Performance Near-infrared Photodetector. *Nano Energy* **2016**, *25*, 34−41. (c) Amador-Alvarado, S.; Flores-Camacho, J. M.; Solis-Zamudio, A.; Castro-Garcia, R.; Perez-Huerta, J. S.; Antunez-Ceron, E.; Ortega-Gallegos, J.; Madrigal-Melchor, J.; Agarwal, V.; Ariza-Flores, D. Temperature-dependent Infrared Ellipsometry of Mo-doped VO(2) Thin Films Across the Insulator to Metal Transition. *Sci. Rep.* **2020**, *10* (1), 8555. (d) Huang, Y.; Bai, G.; Zhao, Y.; Xie, H.; Yang, X.; Xu, S. Yb/Ho Codoped Layered Perovskite Bismuth Titanate Microcrystals with Upconversion Luminescence: Fabrication, Characterization, and Application in Optical Fiber Ratiometric Thermometry. *Inorg. Chem.* **2020**, *59* (19), 14229−14235.

(27) (a) Fang, Y.; Dong, Q.; Shao, Y.; Yuan, Y.; Huang, J. Highly Narrowband Perovskite Single- Crystal Photodetectors Enabled by Surface-charge Recombination. *Nat. Photonics* **2015**, *9* (10), 679−686. (b) He, Y.; Hadar, I.; Kanatzidis, M. G. Detecting Ionizing Radiation using Halide Perovskite Semiconductors Processed through Solution and Alternative Methods. *Nat. Photonics* **2022**, *16* (1), 14−26. (c) Lin, Q.; Armin, A.; Burn, P. L.; Meredith, P. Filterless Narrowband Visible Photodetectors. *Nat. Photonics* **2015**, *9* (10), 687−694. (d) Dong, Q.; Fang, Y.; Shao, Y.; Mulligan, P.; Qiu, J.; Cao, L.; Huang, J. Electron-hole Diffusion Lengths > 175 μm in Solution-grown CH3NH3PbI3 Single Crystals. *Science* **2015**, *347*, 967−970.

(28) (a) Jedlicka, E.; Wang, J.; Mutch, J.; Jung, Y. K.; Went, P.; Mohammed, J.; Ziffer, M.; Giridharagopal, R.; Walsh, A.; Chu, J. H.; et al. Bismuth Doping Alters Structural Phase Transitions in Methylammonium Lead Tribromide Single Crystals. *J. Phys. Chem. Lett.* **2021**, *12* (11), 2749−2755. (b) Meng, R.; Wu, G.; Zhou, J.; Zhou, H.; Fang, H.; Loi, M. A.; Zhang, Y. Understanding the Impact of Bismuth Heterovalent Doping on the Structural and Photophysical Properties of CH3NH3PbBr3 Halide Perovskite Crystals with Near-IR Photoluminescence. *Chemistry* **2019**, *25* (21), 5480−5488. (c) Li, C.; Chen, X.; Li, N.; Liu, J.; Yuan, B.; Li, Y.; Wang, M.; Xu, F.; Wu, Y.; Cao, B. Highly Conductive N-type CH3NH3PbI3 Single Crystals Doped with Bismuth Donors. *J. Mater. Chem. C* **2020**, *8* (11), 3694−3704.

(29) (a) Li, J.-L.; Yang, J.; Wu, T.; Wei, S.-H. Formation of DY Center as N-type Limiting Defects in Octahedral Semiconductors: the Case of Bi-doped Hybrid Halide Perovskites. *J. Mater. Chem. C* **2019**, *7* (14), 4230−4234. (b) Zhang, Z.; Ren, L.; Yan, H.; Guo, S.; Wang, S.; Wang, M.; Jin, K. Bandgap Narrowing in Bi-Doped CH3NH3PbCl3 Perovskite Single Crystals and Thin Films. *J. Phys. Chem. C* **2017**, *121* (32), 17436−17441.

(30) Saidaminov, M. I.; Abdelhady, A. L.; Murali, B.; Alarousu, E.; Burlakov, V. M.; Peng, W.; Dursun, I.; Wang, L.; He, Y.; Maculan, G.; et al. High-quality Bulk Hybrid Perovskite Single Crystals within Minutes by Inverse Temperature Crystallization. *Nat. Commun.* **2015**, *6*, 7586.

(31) Yamada, Y.; Hoyano, M.; Akashi, R.; Oto, K.; Kanemitsu, Y. Impact of Chemical Doping on Optical Responses in Bismuth-Doped CH(3)NH(3)PbBr(3) Single Crystals: Carrier Lifetime and Photon Recycling. *J. Phys. Chem. Lett.* **2017**, *8* (23), 5798−5803.

(32) (a) Li, Y.; Xu, X.; Wang, C.; Ecker, B.; Yang, J.; Huang, J.; Gao, Y. Light-Induced Degradation of CH3NH3PbI3 Hybrid Perovskite Thin Film. *J. Phys. Chem. C* **2017**, *121* (7), 3904−3910. (b) Cai, M.; Ishida, N.; Li, X.; Yang, X.; Noda, T.; Wu, Y.; Xie, F.; Naito, H.; Fujita, D.; Han, L. Control of Electrical Potential Distribution for High-Performance Perovskite Solar Cells. *Joule* **2018**, *2* (2), 296−306. (c) Zhang, M.; Chen, Q.; Xue, R.; Zhan, Y.; Wang, C.; Lai, J.; Yang, J.; Lin, H.; Yao, J.; Li, Y.; et al. Reconfiguration of Interfacial Energy Band Structure for High-performance Inverted Structure Perovskite Solar Cells. *Nat. Commun.* **2019**, *10* (1), 4593.

(33) Lei, Y.; Chen, Y.; Zhang, R.; Li, Y.; Yan, Q.; Lee, S.; Yu, Y.; Tsai, H.; Choi, W.; Wang, K.; et al. A Fabrication Process for Flexible Single-crystal Perovskite Devices. *Nature* **2020**, *583* (7818), 790−795.

(34) (a) Chen, Y.; Lei, Y.; Li, Y.; Yu, Y.; Cai, J.; Chiu, M. H.; Rao, R.; Gu, Y.; Wang, C.; Choi, W.; et al. Strain Engineering and Epitaxial Stabilization of Halide Perovskites. *Nature* **2020**, *577* (7789), 209−215. (b) Chen, Y.; Yi, H. T.; Wu, X.; Haroldson, R.; Gartstein, Y. N.; Rodionov, Y. I.; Tikhonov, K. S.; Zakhidov, A.; Zhu, X. Y.; Podzorov, V. Extended Carrier Lifetimes and Diffusion in Hybrid Perovskites Revealed by Hall Effect and Photoconductivity Measurements. *Nat. Commun.* **2016**, *7*, 12253.

(35) Han, T. H.; Tan, S.; Xue, J.; Meng, L.; Lee, J. W.; Yang, Y. Interface and Defect Engineering for Metal Halide Perovskite Optoelectronic Devices. *Adv. Mater.* **2019**, *31* (47), No. e1803515.

(36) (a) Yakunin, S.; Dirin, D. N.; Shynkarenko, Y.; Morad, V.; Cherniukh, I.; Nazarenko, O.; Kreil, D.; Nauser, T.; Kovalenko, M. V. Detection of Gamma Photons using Solution-Grown Single Crystals of Hybrid Lead Halide Perovskites. *Nat. Photonics* **2016**, *10* (9), 585−589. (b) Wei, H.; DeSantis, D.; Wei, W.; Deng, Y.; Guo, D.; Savenije, T. J.; Cao, L.; Huang, J. Dopant Compensation in Alloyed CH3NH3PbBr3-xClx Perovskite Single Crystals for Gamma-ray Spectroscopy. *Nat. Mater.* **2017**, *16* (8), 826−833.

(37) (a) Reihani, A.; Lim, J. W.; Fork, D. K.; Meyhofer, E.; Reddy, P. Microwatt-Resolution Calorimeter for Studying the Reaction Thermodynamics of Nanomaterials at High Temperature and Pressure. *ACS Sens.* **2021**, *6* (2), 387−398. (b) Sadat, S.; Meyhofer, E.; Reddy, P. High Resolution Resistive Thermometry for Micro/nanoscale Measurements. *Rev. Sci. Instrum.* **2012**, *83* (8), 084902.

(38) (a) Wu, X.; Zhou, B.; Zhou, J.; Chen, Y.; Chu, Y.; Huang, J. Distinguishable Detection of Ultraviolet, Visible, and Infrared Spectrum with High-Responsivity Perovskite-Based Flexible Photosensors. *Small* **2018**, *14* (19), No. e1800527. (b) Alwadai, N.; Haque, M. A.; Mitra, S.; Flemban, T.; Pak, Y.; Wu, T.; Roqan, I. High-Performance Ultraviolet- to-Infrared Broadband Perovskite Photodetectors Achieved via Inter-/Intraband Transitions. *ACS Appl. Mater. Interfaces* **2017**, *9* (43), 37832−37838.

(39) Moreno, M.; Kosarev, A.; Torres, A.; Ambrosio, R. Comparison of Three Un-cooled Micro-bolometers Configurations based on Amorphous Silicon-germanium Thin Films Deposited by Plasma. *J. Non-Cryst. Solids* **2008**, *354* (19−25), 2598−2602.

(40) Kumar, R. T. R.; Karunagaran, B.; Mangalaraj, D.; Narayandass, S. K.; Manoravi, P.; Joseph, M.; Gopal, V.; Madaria, R. K.; Singh, J. P. Room Temperature Deposited Vanadium Oxide Thin Films for Uncooled Infrared Detectors. *Mater. Res. Bull.* **2003**, *38* (7), 1235−1240.

(41) Dong, L.; Yue, R.; Liu, L. An Uncooled Microbolometer Infrared Detector based on Poly- SiGe Thermistor. *Sens. Actuators, A* **2003**, *105* (3), 286−292.

(42) Nandi, S.; Panwar, V.; Misra, A. Metal-carbon Nanotube Composite for Wavelength-selective Bolometer with Improved Characteristics. *J. Appl. Phys.* **2023**, *133* (4), 043104.

(43) Guyot-Sionnest, P.; Roberts, J. A. Background Limited Mid-infrared Photodetection with Photovoltaic HgTe Colloidal Quantum Dots. *Appl. Phys. Lett.* **2015**, *107* (25), 253104.

(44) Park, J.; Al Mahfuz, M. M.; Huebner, R.; Ko, D.-K. Uncooled Mid-Wavelength Infrared Photoconductive Detectors Based on PbSe Nanocrystals. *ACS Appl. Electron. Mater.* **2023**, *5* (4), 2386−2393.

(45) Qiu, J.; Liu, Y.; Cai, Z.; Phan, Q.; Shi, Z. CdSe:In Mid-infrared Transparent Conductive Films Prospering Uncooled PbSe/CdSe Heterojunction Photovoltaic Detectors. *Mater. Adv.* **2022**, *3* (2), 1079−1086.

https://doi.org/10.1021/acsami.3c13305
ACS Appl. Mater. Interfaces 2023, 15, 56526−56536

(46) (a) Lampert, M. A. Simplified Theory of Space-Charge-Limited Currents in an Insulator with Traps. *Phys. Rev.* **1956**, *103* (6), 1648−1656. (b) Duijnstee, E. A.; Ball, J. M.; Le Corre, V. M.; Koster, L. J. A.; Snaith, H. J.; Lim, J. Toward Understanding Space-Charge Limited Current Measurements on Metal Halide Perovskites. *ACS Energy Lett.* **2020**, *5* (2), 376−384.

https://doi.org/10.1021/acsami.3c13305
ACS Appl. Mater. Interfaces 2023, 15, 56526−56536